Direct-Vlasov Study of Electron Cooling Mechanisms in Paraxial, Unmagnetized Plasma Thruster Plumes

IEPC-2017-104

Presented at the 35th International Electric Propulsion Conference
Georgia Institute of Technology – Atlanta, Georgia – USA
October 8–12, 2017

Mario Merino,* Javier Mauriño† and Eduardo Ahedo‡
Equipo de Propulsión Espacial y Plasmas (EP2), Universidad Carlos III de Madrid, Leganés, Spain

A model of an unmagnetized, steady-state, paraxial, collisionless, quasineutral plasma plume expanding into vacuum is presented. Electrons are treated kinetically, relying on the first-order conservation of their averaged radial action integral for the integration of Vlasov's equation, whereas ions are treated as a cold species. The quasi-2D behavior of plasma density; self-consistent electric potential; electron pressure, and temperature is analyzed. In particular, the model yields the electron cooling rate in the collisionless plume, which differs from the Boltzmann relation or polytropic laws usually employed in fluid and PIC/fluid hybrid plume models. A simplified polytropic law is derived that is consistent with the kinetic electron expansion, which can replace current models in electric space propulsion plasma-spacecraft interaction codes.

I. Introduction

THE operation of electric space propulsion systems such as the gridded ion thruster (GIT) and the Hall effect thruster (HET) results in the directed expansion of a plasma into vacuum, consisting of hypersonic ions with velocities in the order of tens of km/s and subthermal electrons with temperatures of a few eV. These plasma plumes can interact mechanically, chemically, and electrically with nearby objects, potentially damaging or contaminating their surfaces[1–4]. This affects, in particular, solar arrays and other appendages. When in operation, the plasma emitted by electric thrusters is also the main factor that sets up the electric charge and potential of the whole spacecraft, compared to the more tenuous environmental plasma and the photoelectric effect on sunlit surfaces[5, 6]. Consequently, electric propulsion plasma plumes play an important role in space systems engineering and constitute a serious concern for satellite integrators. Plasmas expanding into vacuum are also transversal to many different fields, such as plasma material processing[7, 8] and astrophysics[9].

Plasma plumes have therefore been extensively researched in the laboratory[10–17] and in space[18–22]. Existing experimental data shows the monotonic decrease of plasma density, electron temperature and electric potential along the expansion. In the near-region, which extends for the first few thruster radii outside of the thruster, residual electric and magnetic fields from the thruster, collisions with the larger concentration of neutrals there, and three-dimensional non-homogeneities resulting from the geometry of the thruster and its neutralizer exert an important influence on the plasma dynamics[12, 13, 23, 24]. Farther downstream, in the far-region, these effects become negligible, the inhomogeneities in the radial density profile smooth out, and the plasma is near-collisionless, unmagnetized, and quasineutral[11, 16, 17, 25, 26].

Together with these experimental observations, the present understanding of plasma plumes stems from models. Full particle-in-cell (PIC) approaches have been used to study the expansion of rarefied plasmas with mixed success: while this method yields great physical detail, the extent of the plume domain and the reduced time scale of electron motion make them impractical except for some specialized studies[27–29].

---

*Assistant Professor, Aerospace Engineering department, mario.merino@uc3m.es.
†Visiting student, Imperial College, UK.
‡Professor, Aerospace Engineering department, eduardo.ahedo@uc3m.es.

Moreover, the expansion causes the number of numerical particles per cell to decrease downstream, resulting in high statistical noise and regularization problems. Multi-fluid models, on the other hand, enable the quick estimation of the plasma properties in the plume[26, 30, 31], but have limited accuracy when dealing with a near-collisionless medium, as they require external closure relations to truncate the infinite series of fluid equations, and do not provide the kinetic plasma response. Hybrid PIC/fluid models, which treat the heavy species as particles and the electrons as a fluid, combine some of the advantages of each approach[32–38]. This third way to study plasma plumes has thus become popular in the last decades, with multiple examples of hybrid codes being developed.

The need of a closure relation for electrons affects multi-fluid and hybrid models both, and is one of their major downsides. Such closure is commonly applied at the pressure-tensor level, although approaches at the heat flux level also exist[1, 39]. The most extended model relies on Boltzmann's relation, which results in isotropic, isothermal electrons[35, 39]. Unfortunately, while Boltzmann's relation is adequate for a confined electron population, and thus it is a valid approximation in the first part of the expansion, it fails to predict the electric potential fall along the plume, which is infinite in the Boltzmann model. A small improvement over that closure is to treat the electrons as a polytropic species[15, 26, 30, 40], which cools down at a rate given by the cooling exponent γ, i.e., $T_e \propto n_e^{\gamma-1}$. While this model yields a finite electric potential fall in the plume, and can to some extent recover the electron temperature drop with the expansion, the self-consistent determination of this new parameter remains an open problem. Clearly, only a kinetic electron model can provide a satisfactory closure relation for fluid electrons.

This paper presents a quasi-2D kinetic plasma plume model and uses it to characterize the electron features of the expansion. The model assumes a collisionless, unmagnetized, quasineutral, steady-state plasma, providing a good description of the far-region plume. The integration of the model relies on the first-order conservation of an averaged action integral of the electron motion, which is an adiabatic invariant under the assumption of low plume divergence angle[41]. This invariant plays an analogous role to the magnetic moment in the magnetized plasma expansion in a magnetic nozzle[42–44]. The electron velocity distribution function (EVDF) is recovered in the plume and the evolution of its lower moments along the expansion is discussed. The collisionless cooling of electrons is studied in detail, and a simplified, 'lumped' polytropic model that respects the total potential fall of the kinetic solution is proposed that can inform multi-fluid and hybrid codes.

The rest of the paper is structured as follows. Section II introduces the general kinetic plasma plume model. This sets up a framework for solving the plasma expansion, which is particularized in Section III for the case of a plasma plume with a radially-parabolic electric potential. Section IV presents the numerical results of the plasma expansion. Then, in Section V the simplified electron cooling model based on a polytropic cooling law is proposed. Finally, Section VI presents some additional comments on the kinetic model in the light of the obtained results, including a discussion of its limits of validity, and Section VII gathers the main conclusions of this work.

II.   General kinetic plasma plume model

The kinetic model of a plasma plume expanding into vacuum consists of combined electron ('e') and ion ('i') submodels as described below, which are used iteratively to find the self-consistent electric potential response. The plume is assumed to be steady-state, axisymmetric, non-rotating, quasineutral, collisionless and unmagnetized. These conditions are well satisfied in the far-region plume of common thrusters like GITs and HETs, after the collisions with neutrals, thruster electromagnetic fields, and 3D features existing around the thruster become irrelevant as described in the Introduction.

The electric potential in a plasma plume decreases axially and radially, accelerating all ions downstream and confining most of the electrons, as sketched in Fig. 1. In this model, the electric potential is assumed to confine all electrons radially, and that only the most energetic electrons overcome the axial potential fall and escape downstream, to offset the ion current and produce a current-free plume.

The expansion is also required to be paraxial, i.e., slowly diverging. This condition allows writing the self-consistent electric potential as

$$\phi = \phi\left(\varepsilon z, r\right), \tag{1}$$

with $\varepsilon \ll 1$. In other words, the axial derivatives of ϕ are distinctly smaller than radial derivatives in the plume. Under these assumptions, electrons typically perform many radial and azimuthal orbits before experiencing an important axial change of the electric potential.
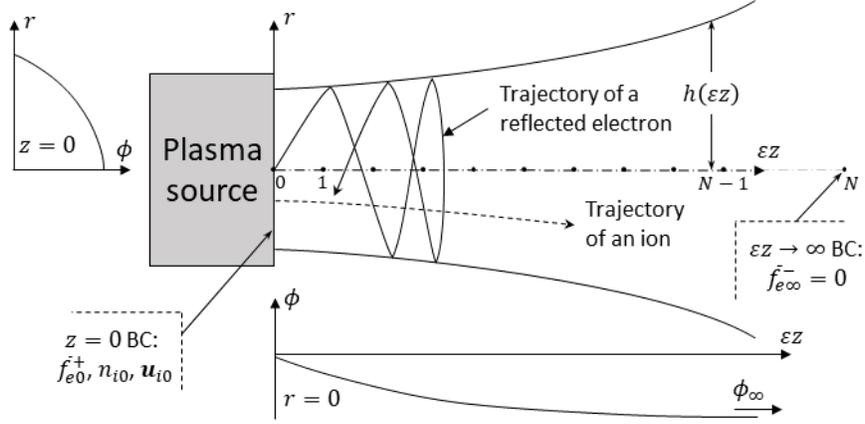
Figure 1. Sketch of the plasma plume expansion from an initial plane $z = 0$ (the upstream model boundary) to $z \to \infty$ (downstream boundary). The electric potential ϕ decreases gently in the axial direction to an asymptotic value ϕ_∞, and faster in the radial direction. Examples of ion and electron trajectories are shown. The outer solid lines represent the characteristic radius of the plume at each z position, $h(\varepsilon z)$. The N dots on the plume axis denote the evaluation nodes used in the model of Section **III**.

A. Electron model

The Hamiltonian of an electron in the steady-state, axisymmetric, paraxial electric potential ϕ can be written as:

$$H = \frac{1}{2m_e}\left(p_z^2 + p_r^2 + \frac{p_\theta^2}{r^2}\right) - e\phi\left(\varepsilon z, r\right), \tag{2}$$

where $H = H\left(z, r, \theta, p_z, p_r, p_\theta\right)$, with $p_z = m_e v_z$, $p_r = m_e v_r$, and $p_\theta = r m_e v_\theta$. The mechanical energy $E = H$ and the canonical azimuthal momentum p_θ of the electron are conserved quantities of motion.

For $\varepsilon = 0$ (i.e., a zero-divergence plume), ϕ becomes a function of r only, so the Hamiltonian has no dependency on z, and p_z is conserved. The perpendicular and axial energies are then independent invariants:

$$E_\perp = \frac{1}{2m_e}\left(p_r^2 + \frac{p_\theta}{r^2}\right) - e\phi(r), \tag{3}$$

$$E_z = E - E_\perp. \tag{4}$$

As electrons are radially trapped by $\phi(r)$, each of them bounces back and forth between certain limit values r_- and r_+ while moving in the z and θ directions. The radial action integral can be defined along one such radial orbit:

$$J_r = \oint p_r \mathrm{d}r, \tag{5}$$

and is another conserved quantity of motion. The conjugated Hamilton-Jacobi phase-angle variable that parametrizes the radial motion is

$$\beta_r = \frac{\partial}{\partial J_r}\int p_r \mathrm{d}r = m_e \frac{\partial H}{\partial J_r}\int \frac{\mathrm{d}r}{p_r}. \tag{6}$$

The variable β_r grows linearly with time and increases in 1 unit every full radial orbit, with $\dot{\beta}_r = \partial H/\partial J_r$. Finally, under these conditions, it is possible to write the Hamiltonian as a function of p_z, J_r, and p_θ only. Incidentally, the conservation of J_r holds exactly also for separable electric potentials of the form $\phi = \phi_z(z) + \phi_r(r)$.

For $0 < \varepsilon \ll 1$, E_z and $E_\perp$ are not independently conserved, and energy can indeed flow between the perpendicular directions of motion (r, θ) and the axial one (z). The definitions of J_r and β_r of Eqs. (5) and (6) may nevertheless still be used, by treating z, p_z as constants inside the integrals. Now, however, J_r varies in time, with

$$\dot{J}_r = \oint e\frac{\partial \phi}{\partial z}\frac{p_z}{p_r}\mathrm{d}r - e\frac{\partial \phi}{\partial z}\oint \frac{p_z}{p_r}\mathrm{d}r, \tag{7}$$

Likewise, β_r no longer increases linearly in time:

$$\dot{\beta}_r = \frac{\partial H}{\partial J_r} \left(1 - \int e \frac{\partial \phi}{\partial z} \frac{m_e p_z}{p_r^3} \mathrm{d}r + e \frac{\partial \phi}{\partial z} \int \frac{m_e p_z}{p_r^3} \mathrm{d}r \right).$$

Additionally, the relation between E and p_z, J_r and p_θ codified in the Hamiltonian now also has a dependency on z at order ε,

$$E = E\left(z, p_z, J_r, p_\theta\right). \tag{8}$$

Notwithstanding this, action integrals like J_r are *adiabatic invariants* under small perturbations[45]. This means that, while J_r can have *periodic* variations of order ε, its *secular* changes are only of order ε^2 or higher, as can be shown by detailed inspection of the time integral of Eq. (7). Likewise, $\dot{\beta}_r$ in Eq. (8) has only periodic variations to order β_r. The conservation of E, p_θ and the adiabatic invariance of J_r can be exploited to simplify the solution of the electron kinetic equation. The electron velocity distribution function f_e is decomposed into a β_r-averaged value $\bar{f}_e$ plus an oscillation $\hat{f}_e$ about this average:

$$f_e = \bar{f}_e\left(z, E, J_r, p_\theta\right) + \hat{f}_e\left(z, \beta_r, E, J_r, p_\theta\right), \tag{9}$$

with $\bar{f}_e = \int_0^1 f_e \mathrm{d}\beta_r$ and $\int_0^1 \hat{f}_e \mathrm{d}\beta_r = 0$. Since the chosen variables do not discriminate between electrons with positive or negative axial velocity, whenever this distinction is necessary, $\bar{f}_e$ and $\hat{f}_e$ are further split as $\bar{f}_e = \bar{f}_e^+ + \bar{f}_e^-$, $\hat{f}_e = \hat{f}_e^+ + \hat{f}_e^-$, where superscript '+' indicates $v_z \geqslant 0$, and '−,' $v_z < 0$.

The complete electron Vlasov equation for electrons then reads:

$$v_z \frac{\partial f_e}{\partial z} + \dot{\beta}_r \frac{\partial \hat{f}_e}{\partial \beta_r} + \dot{J}_r \frac{\partial f_e}{\partial J_r} = 0. \tag{10}$$

Integration of this equation requires boundary conditions $\bar{f}_{e0}^+, \hat{f}_{e0}^+$ at $z = 0$, which we refer to as upstream or *source electrons*, and $\bar{f}_{e\infty}^-, \hat{f}_{e\infty}^-$ at $z \to \infty$, i.e., downstream or *background electrons*. For a plasma plume expanding into vacuum, there are no background electrons, i.e. $\bar{f}_{e\infty}^-, \hat{f}_{e\infty}^- = 0$.

Actual plasma sources are expected to deliver an electron population that is near-homogeneous in β_r, so that $\hat{f}_{e0}^+ = O(\varepsilon)$; in particular, for initially semi-Maxwellian electrons, $\hat{f}_{e0}^+$ is strictly 0. If $\hat{f}_{e0}^+$ is of order ε, then $\hat{f}_e$ is also of order ε inside the plasma plume domain. Hence, we can establish the following ordering in the plasma plume,

$$\bar{f}_e = O\left(1\right); \quad \hat{f}_e = O\left(\varepsilon\right). \tag{11}$$

Then, after averaging over β_r, Eq. (10) becomes,

$$v_z \frac{\partial \bar{f}_e}{\partial z} = O\left(\varepsilon^2\right), \tag{12}$$

This means that, up to order ε, $\bar{f}_e$ is constant along z for each combination of E, J_r, p_θ, in regions delimited by the axial turning manifold $v_z = 0$, whose expression must be obtained by inversion of Eq. (8):

$$p_z\left(z, E, J_r, p_\theta\right) = 0. \tag{13}$$

The phase space beyond this manifold is energetically forbidden.

In general, Eq. (13) has a non-monotonic behavior in the z direction, which results from two competing effects on the electron motion: on the one hand, the axially-decreasing electric potential causes a confining force that pushes electrons upstream. On the other hand, in the expanding electric potential, the adiabatic invariance of J_r and the conservation of p_θ create a net axial force on the radially-averaged electron motion that pushes them downstream. This phenomenon is analogous to the magnetic mirror effect in a magnetized plasma, which pushes electrons in the direction of the expanding magnetic field due to the invariance of the magnetic moment of the electron. Consequently, the turning manifold can divide the solution existence domain into regions of four different types, or equivalently, the electrons into four subpopulations, according to their connectivity with the upstream and downstream boundaries:

1. Regions that connect with both upstream and downstream boundaries. In these regions, electrons have enough energy to overcome all potential barriers and reach the opposite boundary without any reflections, and they are therefore termed *free electrons*. Hence, $\bar{f}_{e(1)}^+ = \bar{f}_{e0}^+$, $\bar{f}_{e(1)}^- = \bar{f}_{e\infty}^-$ in the free electron region.

2. Electrons in regions connected only with the upstream boundary eventually turn back and return to the source. They are called *reflected electrons*. In these regions, $\bar{f}_{e(2)}^+ = \bar{f}_{e(2)}^- = \bar{f}_{e0}^+$.

3. Similarly, there are regions only connected with the downstream boundary. Therefore, for a plasma plume expanding into vacuum $\bar{f}_{e(3)}^+ = \bar{f}_{e(3)}^- = \bar{f}_{e\infty}^- \equiv 0$, and these are *empty regions*.

4. Lastly, regions of existence that are not connected with either the upstream or downstream boundaries may contain *doubly-trapped* electrons. Here, $\bar{f}_{e(4)}^+ = \bar{f}_{e(4)}^-$, but the value of the distribution function in these regions remains otherwise undetermined, and the solution requires additional information from outside of the present kinetic model. As discussed in Section VI, physical reasoning suggests that these regions must be populated by a f_e that is near-Maxwellian and near-continuous with neighboring parts of phase space.

To obtain the β_r-dependent part of the distribution function, $\hat{f}_e$, to comparable accuracy, it is necessary to tackle the rest of the non-averaged Vlasov Eq. (10) up to order ε, i.e.,

$$v_z \frac{\partial \hat{f}_e}{\partial z} + \frac{\partial H}{\partial J_r} \frac{\partial \hat{f}_e}{\partial \beta_r} = -\dot{J}_r \frac{\partial \bar{f}_e}{\partial J_r} + O\left(\varepsilon^2\right). \tag{14}$$

This correction to f_e is not computed in the present work. As a result, the obtained solution $f_e = \bar{f}_e$ is strictly only accurate to zeroth-order in ε. Once $\bar{f}_e$ is known, any moment of the electron species or of a particular subpopulation, and other standard related quantities such as densities, velocities, and temperatures can be computed as described in Appendix A.

B. Ion model

The ions emitted by a plasma thruster are commonly much colder than the electron population, $T_i \ll T_e$. Additionally, ions are hypersonic[26], with a bulk velocity $\boldsymbol{u}_i$ about 5–40 times larger than the plasma sonic velocity $c_s = \sqrt{T_e/m_i}$. Nonetheless, except for the lightest propellants, $\boldsymbol{u}_i$ is still much less than the electron thermal velocity, $c_e = \sqrt{T_e/m_e}$. Thus, the following ordering of velocities is satisfied in an electric propulsion plasma plume:

$$c_i \ll c_s \ll u_i \ll c_e. \tag{15}$$

Moreover, ions are accelerated downstream by the electric field in the plasma plume, so all of them are *free ions* that undergo no axial reflections. Consequently, their motion is far simpler than that of electrons.

Neglecting the dispersion in the ion velocity distribution function ($v_i \simeq u_i$), ions are modeled as a cold species that satisfies the following steady-state continuity and momentum equations,

$$\nabla \cdot (n_i \boldsymbol{u}_i) = 0, \tag{16}$$

$$m_i(\boldsymbol{u}_i \cdot \nabla)\boldsymbol{u}_i + e\nabla\phi = 0, \tag{17}$$

which must be supplemented with upstream boundary conditions at $z = 0$, n_{i0} and $\boldsymbol{u}_{i0}$.

These hyperbolic equations can be solved numerically for a given ϕ, with Eq. (17) providing $\boldsymbol{u}_i$ by direct propagation of ion trajectories with the method of characteristics. Once $\boldsymbol{u}_i$ is known, discretization of Eq. (16) in the plume domain gives n_i.

C. Self-consistent electric potential determination

The electron and ion models defined above can be used to compute the zeroth-order $n_e, \boldsymbol{u}_e$, and $n_i, \boldsymbol{u}_i$ at any point (z, r) of the plume, given a electric potential map $\phi(\varepsilon z, r)$ and a set of compatible boundary upstream conditions $\bar{f}_{e0}^+$, n_{i0}, and $\boldsymbol{u}_{i0}$. The quasineutrality assumption and current-free condition in the paraxial limit couple the two species together and allow finding the self-consistent plume solution iteratively, including the electric potential ϕ,

$$n_i = n_e; \quad u_{zi} = u_{ze}. \tag{18}$$

Observe that n_e can be decomposed as $n_e = n_e^+ + n_e^-$, where the $+$ and $-$ signs denote the contributions of $\bar{f}_e^+$ and $\bar{f}_e^-$, respectively. Similarly, $u_{ze} = u_{ze}^+ + u_{ze}^-$. Since $\bar{f}_e^-$ at $z = 0$ is part of the solution, only n_e^+ and u_{ze}^+ are known a priori at the upstream boundary. Indeed, the values of n_e^- and u_{ze}^- depend on the fraction

of *reflected electrons* that return to the plasma source. Thus, it is not possible, in general, to determine whether the upstream boundary conditions are compatible with Eqs. (18) at $z = 0$ without solving the electron expansion. To overcome this difficulty, only the shape, but not the magnitude, of $\bar{f}_{e0}^+$ is prescribed:

$$\bar{f}_{e0}^+ = n_{e0}^+ \bar{F}_{e0}^+ \tag{19}$$

where F_{e0}^+ is the specified normalized distribution function, and n_{e0}^+, is the magnitude of $\bar{f}_{e0}^+$ to be computed as part of the solution.

An iterative solution procedure can then be established as follows. The value of ϕ is fixed at the origin, where $\phi(0,0) = 0$ is chosen. Then, an initial guess of the functions ϕ and n_{e0}^+ is produced. The electron and ion models are solved to obtain n_e, u_{ze}, n_i, u_{zi} at a set of evaluation nodes (z_i, r_i) for $i = 1, \ldots, N$. Equations (18) at those points provide $2N$ error equations to be zeroed. Next, a new guess of ϕ and n_{e0}^+ is generated to lower this error, and the procedure is repeated until convergence with a prescribed tolerance is achieved. Upon completion, the solution method yields the self-consistent ϕ and n_{e0}^+ functions.

III.   Radially-parabolic electric potential

Applying a constraint on the radial shape of the electric potential allows reducing the electron integrals of J_r and β_r in Eqs. (5) and (6) to closed forms, simplifying the solution process. In this section, solutions with a radially-parabolic potential are sought,

$$\phi(h, r) = -\frac{T_e^* h_0^2}{e h^4} r^2 + \phi_z(h), \tag{20}$$

where $h(\varepsilon z)$ is a monotonically-increasing function that represents the (unknown) characteristic radius of the plasma plume at each axial position z, and is used to replace z as the independent variable of the problem, with $h(0) = h_0$. In expression (20), $\phi_z(h)$ is the value of the electric potential along the plume axis, which will be computed by coupling together the electron and ion models as discussed above, and T_e^* is an arbitrary energy constant. The radial electron density profile of Eq. (20) corresponds to a Gaussian density profile $n_e \propto \exp(-r^2/h_0^2)$ in the limit of isothermal electrons with temperature T_e^*. Such radial profile is a reasonable model of the far-region plasma plume that agrees well with experimental measurements of many GITs and HETs[26]. Observe that the non-separability of ϕ stems from first term in the right hand side of Eq. (20) only.

For this electric potential, the corresponding expression for J_r is

$$\frac{J_r}{\pi} = \sqrt{\frac{m_e}{2T_e^*}} \frac{h^2}{h_0} \left[\frac{1}{2m_e} \left(p_r^2 + \frac{p_\theta^2}{r^2} \right) + \frac{T_e^* h_0^2}{h^4} r^2 \right] - |p_\theta|. \tag{21}$$

For compactness, the *perpendicular momentum* is defined as

$$p_\perp = \frac{J_r}{\pi} + |p_\theta|. \tag{22}$$

Then, β_r is related to r through:

$$\cos(2\pi\beta_r) = \frac{p_\perp - \sqrt{2T_e^* m_e} h_0 r^2 / h^2}{\sqrt{p_\perp^2 - p_\theta^2}}, \tag{23}$$

and the extreme values of r in a radial electron orbit, r_+ and r_-, are given by

$$\frac{r_\pm^2}{h^2} = \frac{p_\perp \pm \sqrt{p_\perp^2 - p_\theta^2}}{\sqrt{2T_e^* m_e} h_0}. \tag{24}$$

Equation (13) becomes:

$$\frac{1}{2} m_e v_z^2 = E - U_{\text{eff}}(h, p_\perp) = 0, \tag{25}$$

where U_{eff} is an *effective potential* of the axial electron motion, which depends on J_r and p_θ only through $p_\perp$,

$$U_{\text{eff}}(h, p_\perp) = -e\phi_z(h) + \sqrt{\frac{2T_e^*}{m_e}} \frac{h_0}{h^2} p_\perp. \tag{26}$$

The turning-point manifold of Eq. (25) is illustrated in Fig. 2 for an example function ϕ_z. Inverting Eq. (25) the maximum value of $p_\perp$ for each E and h is given by:

$$p_{\perp M}(h, E) = \sqrt{\frac{m_e}{2T_e^*} \frac{h^2}{h_0} [E + e\phi_z(h)]}.$$

(27)

Locating the extrema of either U_{eff} or $p_{\perp M}$ along h helps define the connectivity of each point of phase space with the upstream and downstream boundary conditions efficiently, and thus dividing it into regions of types 1 to 4 as defined in Section II. Alternatively, Eq. (13) can be analyzed in the $E, p_\perp$ plane, where it has the form of a straight line $s(h)$ for each value of h, proving that the manifold is a ruled surface.
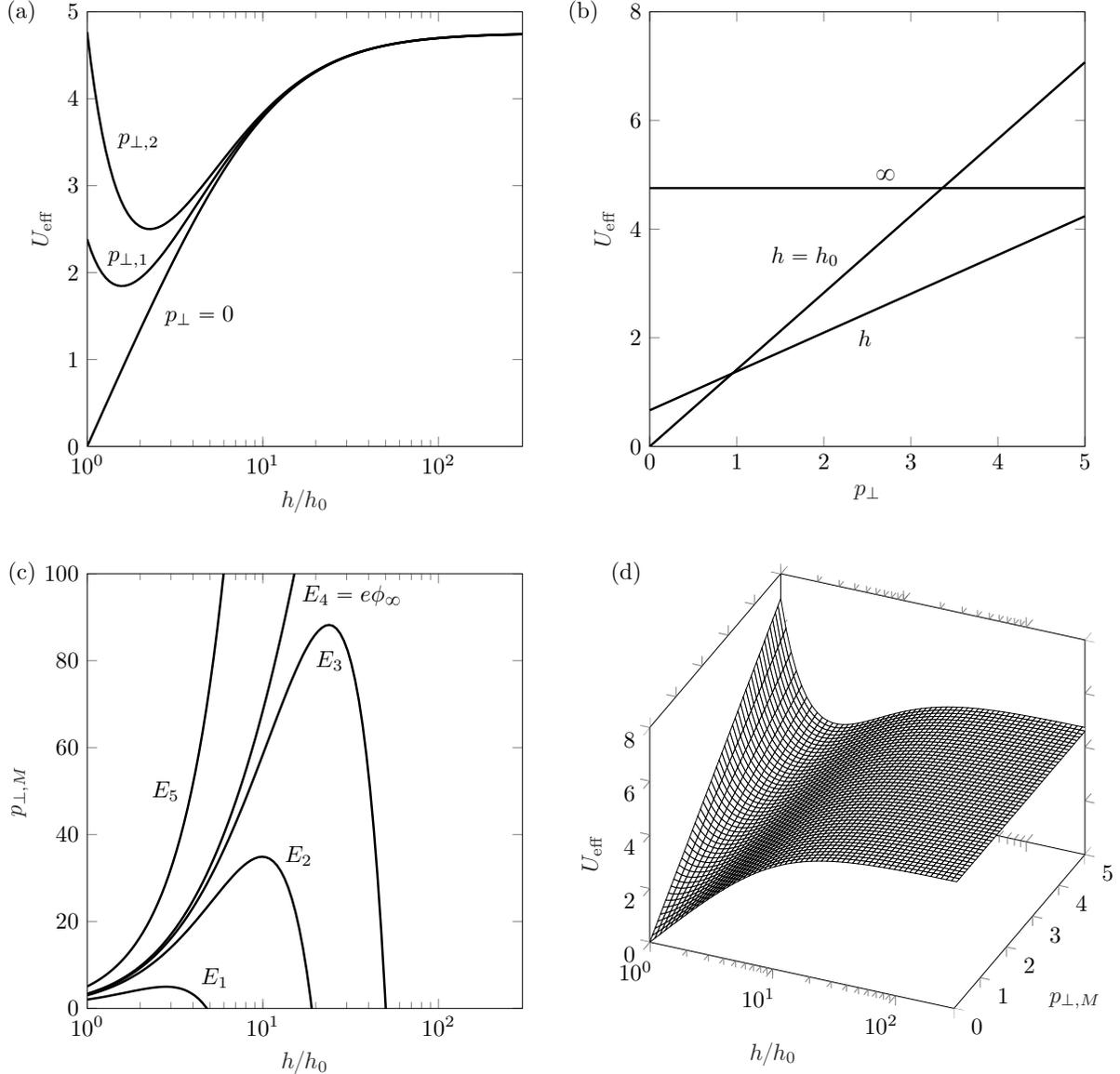

Figure 2. Phase space diagrams for a radially-parabolic electric potential. For the purpose of illustration, the function $\phi_z(h)$ for the case $\chi = 0.02$, $\mu \to \infty$ has been chosen.

As the case of most practical interest, the moment integrals are next particularized for a semi-Maxwellian population upstream in velocity space,

$$\bar{f}_{e0}^+ = f_e^M = 2n_{e0}^+ \left(\frac{m_e}{2\pi T_e^*}\right)^{3/2} \exp\left(-\frac{E}{T_e^*}\right),$$

(28)

where the previously-introduced dimensioning constant T_e^* is the reference temperature. It should be observed that, as $\bar{f}_e^- \neq \bar{f}_e^+$ in general, the initial electron temperature T_{e0} does not coincide with T_e^*. Only in the limit where the free electron population is negligible (and all electrons at the source are reflected electrons) does $T_{e0} \to T_e^*$.

To fully determine the electron distribution function in the doubly-trapped regions while retaining some degree of freedom, it is assumed that they are populated by a fraction of the same Maxwellian distribution function,

$$\bar{f}_{e(4)}^+ = \bar{f}_{e(4)}^- = \alpha f_e^M, \tag{29}$$

where α is a chosen filling factor between 0 and 1.

The moment integrals of the electron species and subpopulations for the radially-parabolic electric potential case, and in particular for the semi-Maxwellian distribution of above, are reduced to compact expressions in the second part of Appendix A.

With regards to ions, under the paraxiallity assumption, the ion continuity Eq. (16) becomes

$$1 = \frac{n_i(h,0)}{n_{i0}(0)} \frac{u_{zi}(h,0)}{u_{zi0}(0)} \frac{h^2}{h_0^2}. \tag{30}$$

Lastly, their momentum Eq. (17) at the plume axis can be integrated into the conservation of ion mechanical energy

$$0 = \frac{1}{2} m_i \left[u_{zi}^2(h,0) - u_{zi0}^2(0) \right] + e\phi_z(h), \tag{31}$$

where $\phi_z(h_0) = 0$ has been prescribed.

The iteration procedure to determine the self-consistent ϕ_z and n_{e0}^+ is simplified by taking the N evaluation nodes at the axis of the plume as shown in Fig. 1, the last of which is taken at $h = \infty$ (i.e., for $z = \infty$). This yields $N - 1$ quasineutrality error equations for the nodes with $h < \infty$, plus a single independent equation from the current-free condition, for a total of N equations. After fixing $\phi_z(h_0) = 0$, there are $N - 1$ unknowns for the discretized $\phi_z(h)$, plus one unknown in n_{e0}^+, for a total of N unknowns. Therefore, the iteration scheme is well-determined. This approach has been implemented into an open source numerical code named AKILES2D[46], after 'Advanced Kinetic Iterative pLasma Expansion Solver 2D.'

The resulting model can be normalized with m_e, e, T_e^*, h_0 and $n_{i0}(0)$. The dimensionless plasma response can be expressed as a function of a dimensionless velocity parameter χ, the ion-electron mass ratio μ, and the filling factor α,

$$\alpha; \quad \chi = \frac{u_{i0}(0)}{\sqrt{T_e^*/m_e}}; \quad \mu = \frac{m_i}{m_e}. \tag{32}$$

Since $u_{i0}(0) = u_{e0}(0)$ from Eq. (18), the parameter χ is also the electron Mach number, or the ratio of ion (or electron) current in the plume to the thermal electron flux (in both cases, based on T_e^* instead of $T_{e0(0)}$). The range of χ from 0.002 to 0.2 covers amply all current and foreseen electric propulsion applications.

Observe that the dependency on μ is only introduced into the problem by Eq. (31). Note that the initial ion Mach number at the axis is related to χ and μ through

$$M_{i0}(0) = \frac{u_{i0}(0)}{\sqrt{T_{e0}(0)/m_i}} = \chi\sqrt{\mu}\frac{T_e^*}{T_{e0}(0)}, \tag{33}$$

where the factor $T_e^*/T_{e0}(0)$ must be computed as part of the solution. For fixed χ, if $\mu \to \infty$ then $M_{i0}(0) \to \infty$ and the ion velocity remains constant in the expansion[26], $u_{zi} = u_{zi0}$. This is the *hypersonic limit*, in which the dependency with μ (or $M_{i0}(0)$) disappears from the problem. Thus, the plasma response in hypersonic electric propulsion plumes depends dominantly on α and χ, while the dependency on μ is negligible.

As a final comment to this section, while the model formulated here has been left as a function of the characteristic plume radius at each actual position, $h(\varepsilon z)$, observe that it is possible to determine the dependency of h on z by integrating the full ion model of Section B without using the paraxial approximation of Eq. (30). Several approximated methods exist to determine the evolution of the characteristic plume radius in hypersonic plasma plumes[26].

IV. Results

The paraxial plasma plume model with the radially-parabolic electric potential and semi-Maxwellian source electrons is integrated next to investigate the plasma expansion into vacuum. The analysis focuses on the case of completely-filled doubly-trapped electron regions ($\alpha = 1$). The study of other regimes is left for future work.

The solution of the electric potential at the plume axis, $\phi_z(h)$, is shown in Fig. 3(a) for $\chi = 0.002, 0.02, 0.2$ and $\mu \to \infty$ (hypersonic limit). In all cases, $\phi_z(h)$ decreases monotonically downstream to an asymptotic value ϕ_∞; most of the potential fall occurs early in the expansion. As it can be observed, increasing χ results in a faster approach to the asymptotic value. The effect of a finite, moderate value of μ on the shape of $\phi_z(h)$ is only noticeable at low values of χ, and causes the potential to approach faster its asymptotic value too. For completness, the 2D electric potential profile for $\chi = 0.02$, $\mu \to \infty$ is illustrated in Fig. 3(b).

The value of ϕ_∞ is plotted as a function of χ in Fig. 4(a). As χ is increased, there is a larger free electron current, and consequently, $e\phi_\infty/T_e^*$ becomes less negative to allow more electrons to escape downstream. As explained in Appendix B, when the condition in Eq. (56) is satisfied, then ϕ_∞ depends only on the value of χ and can be computed from the quasineutrality and current-free conditions at $h = h_0$ only with Eqs. (57). The limit curve of Eq. (56) is displayed in Fig. 3 for comparison with the actual solutions of $\phi_z(h)$. This condition is met for all χ and for the studied range of $10^4 \leqslant \mu < \infty$. Hence, in the presented cases ϕ_z and the rest of magnitudes shown in Fig. 4 (n_{e0}^-/n_{e0}^+, T_{ze0}/T_e^*, $T_{\perp e0}/T_e^*$ and T_{e0}/T_e^*) can be computed before solving the full kinetic problem, and the parameter χ alone then controls the fraction of free electrons in the plasma plume. The limit value of χ for a semi-Maxwellian population upstream is $\sqrt{2/\pi} \simeq 0.8$, for which all electrons at $h = h_0$ are free electrons and no reflected electrons exist ($n_{e0}^- = 0$). In this limit, the electron population at $h = h_0$ is just the semi-Maxwellian in the boundary condition $\bar{f}_{e0}^+$. As it can be observed in Fig. 4, n_{e0}^-/n_{e0}^+ and $T_{ze0}(0)/T_e^*$ decrease with increasing chi, but $T_{\perp e0}(0)/T_e^*$ has a non-monotonic behavior with a minimum value, as it is equal to 1 for a full Maxwellian *and* for the semi-Maxwellian $\bar{f}_{e0}^+$. As a result, the average temperature $T_{e0}(0)/T_e^*$ also displays a minimum. Due to the difference between $\bar{f}_e^+$ and $\bar{f}_e^-$ at $h = h_0$, a small degree of temperature anisotropy already exists at the upstream boundary (not observable in the figures).

For the rest of this section the discussion focuses on the hypersonic limit ($\mu \to \infty$) with $\chi = 0.02$, unless otherwise noted. The evolution of the electron velocity distribution function $\bar{f}_e$ in the $E, p_\perp$ plane is presented in the plots on the left of Fig. 5. The plots on the right provide the corresponding view in the v_z, v_r variables at the plume axis ($r = 0$). At $h = h_0$, only free and reflected electron populations exist. As the plasma expands, the fraction of reflected electrons gradually decreases, doubly-trapped electrons gain relevance, and empty regions appear. As the plume characteristic radius h continues to increase, the doubly-trapped population becomes dominant. Far downstream, as $h \to \infty$ and $\phi_z(h) \to \phi_\infty$, electron density finally drops to zero and the phase space is divided into a forbidden region and an empty region. The straight lines $s(h_0)$ and $s(\infty)$ (and the corresponding transformed curves in velocity variables at the plume axis) are easily identifiable in Fig. 5. As explained in Appendix B, these two lines play a central role in the geometry of phase space.

From Eq. (30) and the quasineutrality assumption, the electron density along the axis in the hypersonic limit is given by

$$\frac{n_e(h,0)}{n_{i0}(0)} = \frac{h_0^2}{h^2}, \tag{34}$$

This is plotted, together with the density of each electron sub-population at the axis, in Fig. 6. The same conclusions on the dominance of each sub-population can be reached as with Fig. 5: initially, reflected electrons dominate, but soon doubly-trapped electrons become the majority. Boltzmann's relation for density, $n_e \propto \exp(e\phi_z/T_e(0))$, which would result from an isothermal expansion, is also plotted for comparison. As it can be observed, Boltzmann's relation is only a valid approximation in the first part of the expansion; downstream, density drops at a faster rate, revealing that electron cooling takes place in that part of the plume. The lower χ is, the larger the region where the (isothermal) Boltzmann's relation adequately describes the expansion, as it approaches a fully-confiend regime without free electrons.

The electron temperature tensor is diagonal to zeroth-order in ε, with:

$$T_{ze}; \quad T_{\perp e} = T_{re}, T_{\theta e}; \tag{35}$$

as defined in the Appendix A. The axial and perpendicular temperatures $T_{ze}, T_{\perp e}$ for the whole electron species and for each subpopulation are plotted in Fig. 7. The average temperature T_e is also shown. For the
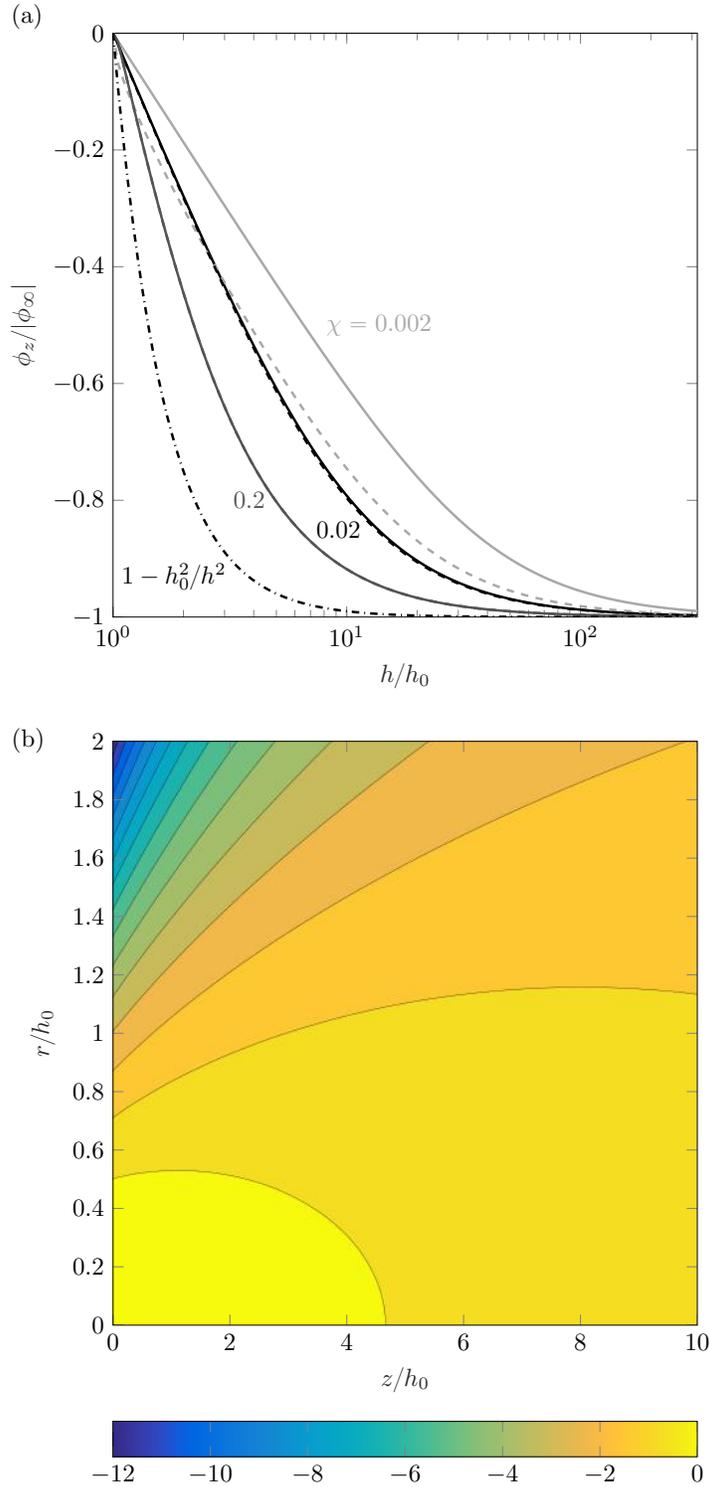
Figure 3. (*a*) **Electric potential** $\phi_z(h)/\phi_\infty$ **along the plume axis for** $\chi = 0.002, 0.02,$ **and** 0.2 **and** $\alpha = 1$. **The solid lines denote the hypersonic limit** $\mu \to \infty$; **the dashed lines have** $\mu = 2.3 \cdot 10^5$ **(corresponding to Xe). The limit curve of Eq. (56) is shown as a thin dash-dot line.** (*b*) **Two-dimensional plot of the electric potential for** $\chi = 0.02, \mu \to \infty, \alpha = 1$. **Thin lines are isopotential lines.**
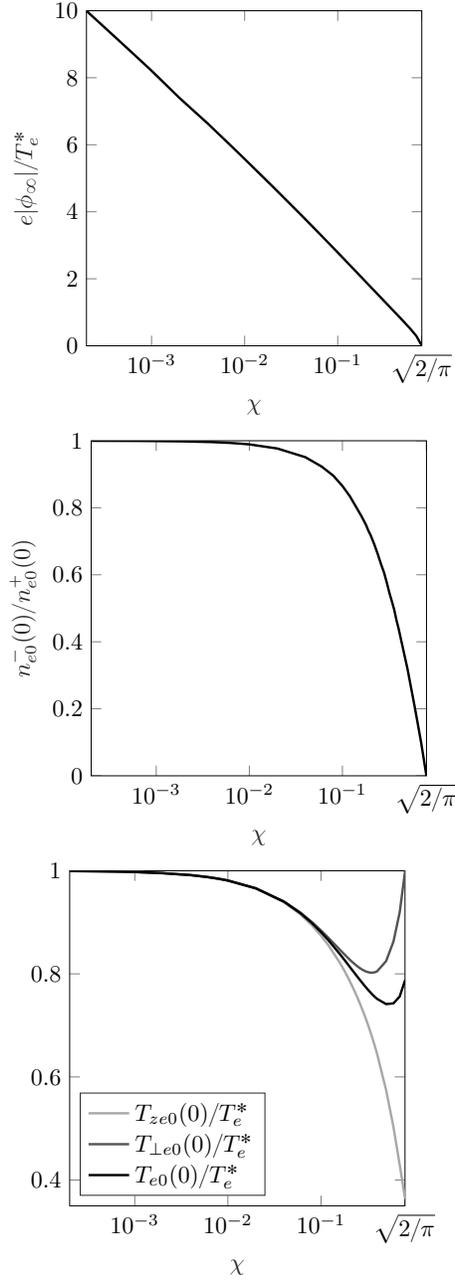
Figure 4. (*a*) **Asymptotic electric potential downstream** ϕ_∞, (*b*) **Reflected electron density ratio** $n_{e0}^-(0)/n_{e0}^+(0)$ **at the upstream boundary condition, and** (*c*) **Initial electron temperature ratios** $T_{ze0}(0)/T_e^*$, $T_{\perp e0}(0)/T_e^*$, $T_{e0}(0)/T_e^*$ **as a function of** χ **for** $\alpha = 1$. **Thin lines correspond to the the solution of Eq.** (57) **for the studied range** $10^4 \leqslant \mu < \infty$.
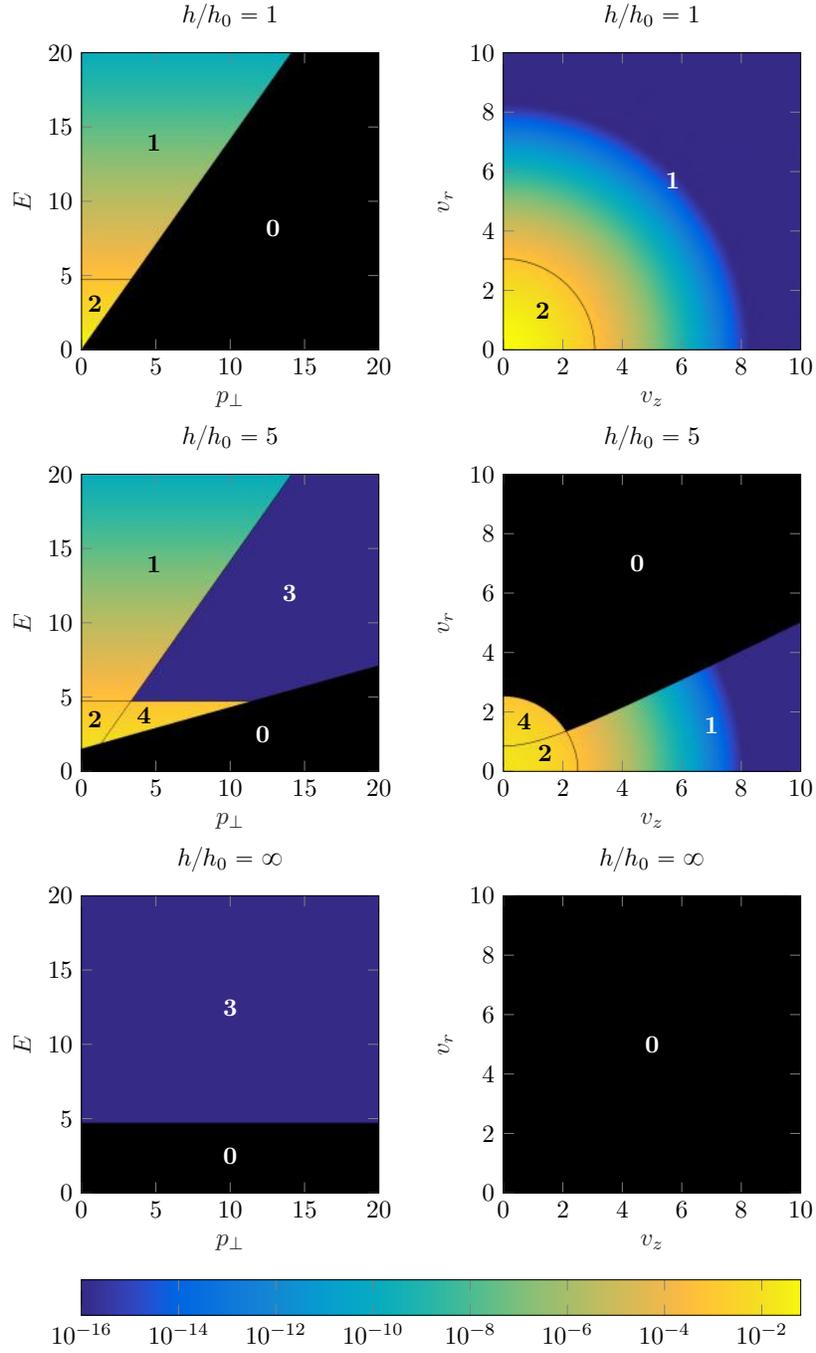
Figure 5. Evolution of the electron velocity distribution function $\bar{f}_e$ at different values of h, for $\chi = 0.02$, $\mu \to \infty$ and $\alpha = 1$. Plots on the left show the $(E, p_\perp)$ plane; those on the right the (v_z, v_r) plane at the plume axis $(r = 0)$. The color map shows the magnitude of $\bar{f}_e^+$. The different regions of phase space are labeled according to the enumeration of Section. A.
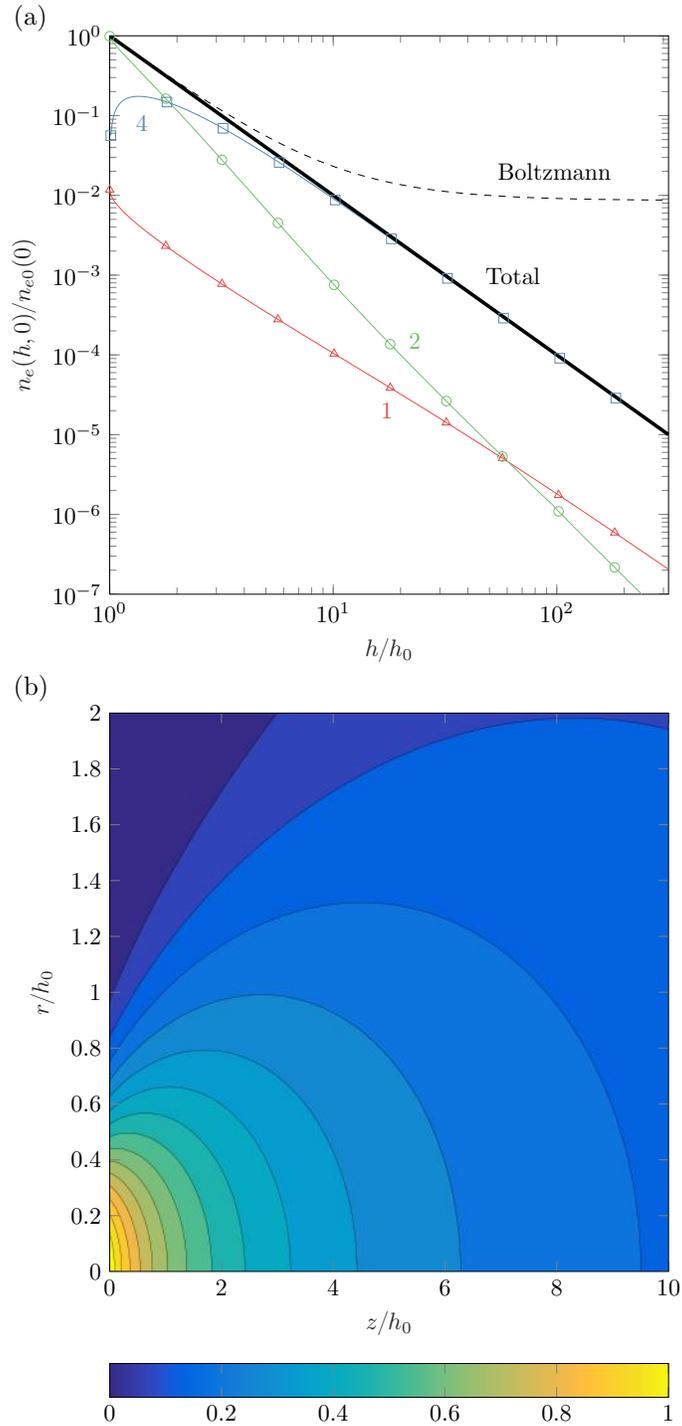
Figure 6. (*a*) Electron density n_e at the plume axis for $\chi = 0.02$, $\mu \to \infty$ and $\alpha = 1$ (thick solid line). The thin lines represent the contributions of free electrons (red, triangles ⎯△⎯), reflected electrons (green, circles ⎯○⎯) and doubly-trapped electrons (blue, squares ⎯□⎯). The dashed line shows Boltzmann's relation for an isothermal electron species with $T_e = T_e^*$ for comparison. (*b*) Two-dimensional plot of the electron density for $\chi = 0.02$, $\mu \to \infty$, $\alpha = 1$. Thin solid lines are contour lines.

whole electron species, both T_{ze} and $T_{\perp e}$ decrease monotonically in the direction of the expansion, but show markedly different behaviors: while T_{ze} tends to an asymptotic value, $T_{\perp e}$ goes to zero. This can be explained by analyzing the evolution of the temperatures of each subspecies. The free electron $T_{ze(1)}$ is nearly constant through the expansion, increasing slowly after a minimum, and eventually dominates downstream. In $T_{\perp e}$, it is the doubly-trapped electrons which dominate nearly everywhere, both in density and in temperature.

The *local* cooling rates for each of the two temperatures and the average temperature are defined as:

$$\gamma_{ze} = \frac{\mathrm{d}\ln T_{ze}}{\mathrm{d}\ln n_e}; \quad \gamma_{\perp e} = \frac{\mathrm{d}\ln T_{\perp e}}{\mathrm{d}\ln n_e}; \quad \gamma_e = \frac{\mathrm{d}\ln T_e}{\mathrm{d}\ln n_e}, \tag{36}$$

and are also plotted in Fig. 7. Free electrons tend to have $\gamma_{ze(1)} \simeq 1$ (i.e., near isothermal) downstream, and actually slightly smaller than 1, consistent with the rising $T_{ze(1)}$, while the perpendicular energy cools down quickly at a rate $\gamma_{\perp e(1)} \simeq 2$. Reflected and doubly-trapped electrons, on the other hand, both tend to a nearly adiabatic (5/3) cooling rate for both temperatures. The initial behavior of the temperatures and cooling exponents near $h = h_0$ is related to the chosen semi-Maxwellian boundary condition and the forbidden region that appears for $v_z \simeq 0$ when the expansion begins, as can be observed in Fig. 5. The behavior of the cooling exponents for the whole electron species results from compounding those of each subpopulation.

While not shown here, the electron temperature in the radial direction is nearly constant. The 2D profile of Fig. 6(b), which showed that plasma density is near-Gaussian in the radial direction, is consistent with a electron population that is essentially isothermal in the radial direction at each plume cross-section.
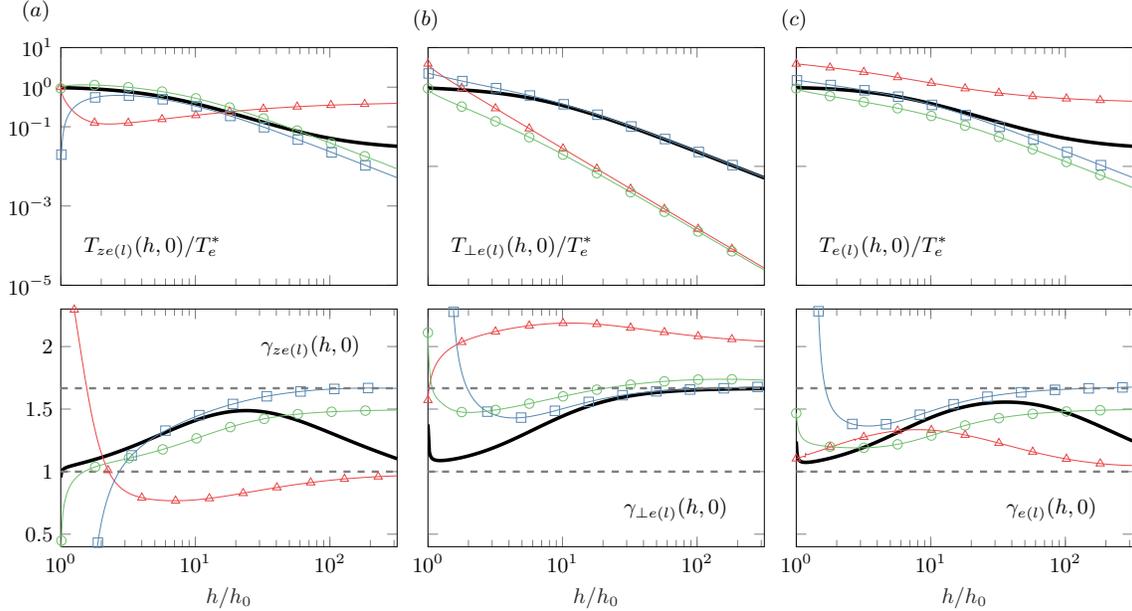

Figure 7. Electron temperature along the plasma plume axis for $\chi = 0.02$, $\mu \to \infty$ and $\alpha = 1$, (a) $T_{ze}(h,0)/T_e^*$, (b) $T_{\perp e}(h,0)/T_e^*$, and (c) $T_e(h,0)/T_e^*$. **Thick black lines represent the temperatures of the global electron population. In each graph, the partial temperatures of free electrons (red triangles —△—), reflected electrons (green circles —○—) and doubly-trapped electrons (blue squares —□—) are also shown. The lower plots depict the corresponding** *local* **cooling exponents** γ_{ze}, $\gamma_{\perp e}$ **and** γ_e. **The dashed lines indicate the limits for an isothermal and an adiabatic population.**

V.   Simple electron cooling model

The results obtained in Section IV can be used to construct closure relations that can inform the fluid electron models of multi-fluid and hybrid codes, replacing Boltzmann's relation and similar laws that are kinetically unjustified in a near-collisionless plasma plume. This can be done with arbitrary level of detail. For example, the average electron temperature can be tabulated against the electron density, and the resulting functional dependency $T_e = T_e(n_e)$ can be used to close the fluid equations at the pressure level.

Alternatively, the temperature tensor *components* can be considered, to take into account the anisotropy of the electron response. Or a closure can be established at the heat-flux level or higher moments of the distribution function.

It is nonetheless desirable to derive a simple, approximate closure relation that can be easily implemented in existing codes. As most codes already feature a simple polytropic cooling law for electrons, an interesting choice is to establish a polytropic electron cooling model with a constant, averaged cooling rate $\bar{\gamma}_e$,

$$\frac{T_e}{T_{e0}(0)} = \left(\frac{n_e}{n_{e0}(0)}\right)^{\bar{\gamma}_e - 1} \tag{37}$$

which respects the electric potential fall ϕ_∞ of the kinetic model. The total electric potential fall ϕ_∞ is a key magnitude of the expansion that affects the interaction of the plasma plume with its environment and any nearby objects such as solar arrays. Since ϕ_∞ is closeley linked to the current of free electrons that escapes downstream, which under the current-free condition must equal the ion current emitted by the thruster, its value is a robust feature of the kinetic model. The 'lumped' polytropic approximation would then at least agree with the kinetic model in that key aspect of the expansion, Note, however, that this model ignores the local variations of the electron cooling rate, and moreover, neglects the anisotropy that exists in the plasma plume.

For a polytropic electron species, the cooling exponent $\bar{\gamma}_e$ and the asymptotic potential fall ϕ_∞ are related through

$$\bar{\gamma}_e = \frac{|e\phi_\infty|}{|e\phi_\infty| - T_{e0}(0)}. \tag{38}$$

The value of $\bar{\gamma}_e$ computed from the ϕ_∞ and $T_{e0}(0)$ of the kinetic solution of Fig. 4 is shown in Fig. 8. The lumped cooling rate is seen to increase with χ, and becomes infinite at $\chi \simeq 0.4$, for which $-e\phi_\infty \to T_{e0}(0)$, hinting that this approximated closure relation is inadequate to model the electron expansion at high values of χ.

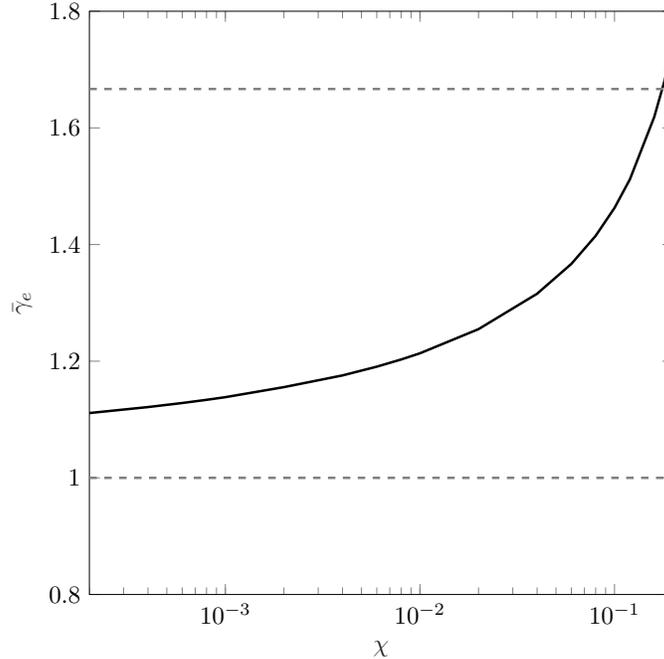**Figure 8.** Lumped polytropic model cooling rate $\bar{\gamma}_e$ that results in the same asymptotic potential fall ϕ_∞ as in the kinetic model as a function of χ for $\alpha = 1$.

VI. Discussion

There are two aspects worth further discussion. Firstly, the kinetic model hinges on the expansion being paraxial. The validity of this assumption is commented on below in Section A. Secondly, the filling of the doubly-trapped electron regions, which are disconnected from both upstream and downstream boundary conditions, cannot be explained from the present steady-state, collisionless model. This issue is commented on in Section B.

A. Validity of the paraxiallity approximation

The validity of the asymptotic expansion in ε of the kinetic electron model relies on the adiabatic invariance of J_r. The degree to which J_r is conserved in each radial orbit depends on the ratio of the radial electron period, $1/\dot{\beta}_r$, to the characteristic time in which an electron experiences changes of the non-separable part of the electric potential as it moves in the axial direction. For an electron in the radially-parabolic potential of Section III, this time is $\sim v_z \varepsilon h_0^2/h^3$, where $dh/dz \sim \varepsilon$ has been taken into account. Proper J_r invariance then requires a small value of this ratio, i.e.,

$$\frac{\varepsilon v_z}{\sqrt{T_e^*/m_e}}\frac{h_0}{h} \ll 1. \tag{39}$$

From this expression, it is possible to extract three conclusions. Firstly, a small value of ε is necessary, as expected. Actual plasma thrusters have divergence half angles in the range of 10–15 deg for GITs to 40–50 deg for HETs. Clearly, the paraxiallity criterion is better satisfied by GITs. Secondly, the conservation of J_r and hence the asymptotic expansion in ε is not uniformly valid in velocity space, as it fails for large v_z. This affects, in particular, the high energy tail in the free electron region. Thirdly, J_r adiabaticity improves as h increases, even if the radial electron period increases with h^2.

Finally, it is noted that the discontinuity in $\bar{f}_e$ that may exist across the boundary between two differently populated regions leads to an infinite gradient that locally breaks the asymptotic expansion in ε. This phenomenon is expected to give rise to a thin layer around the interface, where $\hat{f}_e$ can be of zeroth order. Such discontinuities are inevitable between the free electron region, where $\bar{f}_e^- = 0$, and any other populated region with $\bar{f}_e^+ = \bar{f}_e^-$. The solution of these layers has not been addressed in the present work.

B. On doubly-trapped electron regions

As advanced above, the present model leaves the value of $\bar{f}_e$ undetermined in doubly-trapped regions. A qualitative discussion of two physical mechanisms that may populate them is presented here.

Firstly, collisionality has been neglected in the model, on the basis that the residence time of ions and electrons in the region of interest of the plume is much shorter than the characteristic collision time in the far-region. Nonetheless, while the electron residence time in regions connected to either the upstream or downstream boundary conditions is finite, in doubly-trapped regions it is ideally infinite. This fundamentally affects the time ordering in these regions, and hence the steady state solution in them must be a collisional one for any non-zero plasma collisionality, even if it is arbitrarily small. This could provide a plausible mechanism to populate doubly-trapped regions regions. This argument supports the choice of a Maxwellian or near Maxwellian distribution function for these regions. Another similar population mechanism would be enabled by plasma turbulence.

Secondly, during the transient set-up of the plasma plume, the electric potential changes in time. The energy of an individual electron is not conserved, and decreases a bit on each reflection at the leading expansion front. These two effects combined may result in the trapping of electrons into the doubly-trapped regions as they are being formed. Ongoing work with a non-steady kinetic model in the analogous case of a magnetized plasma expansion suggests that this mechanism can partially fill these regions[44].

VII. Conclusions

A collisionless, paraxial kinetic plasma plume model has been established to investigate the electron expansion. The model exploits the conservation of mechanical energy and angular momentum about the plume axis, and the adiabaticity of the radial action integral, to integrate the electrons Vlasov's equation.

Phase space is seen to be divided into regions of four different types: free electrons, reflected electrons, empty regions, and doubly-trapped electrons.

The evolution of the electric potential, the electron velocity distribution function, and its moments up to the temperature tensor have been analyzed after prescribing a parabolic shape to the radial electric potential profile. The expansion depends on three dimensionless parameters, which describe the free electron electric current, the mass of the ions, and the degree of filling of the doubly-trapped regions.

The collisionless cooling of the electron subpopulations has been analyzed in detail. The local cooling exponents have been computed, and an approximated, lumped polytropic model with exponent $\bar{\gamma}_e$ that is consistent with the total electric potential fall in the kinetic plume model has been proposed that is easy to implement in existing fluid and hybrid simulation codes. The realization that the fraction of free electrons is dictated by ϕ_∞ for the parametric ranges under study allows obtaining ϕ_∞ analytically without solving the whole expansion, and thus the lumped cooling exponent $\bar{\gamma}_e$.

Future work will address higher moments such as the kinetic heat fluxes in the electron population and investigate more accurate lumped models that respect the local cooling and anisotropic behavior of the kinetic model to some extent will be proposed. The effect of partially removing doubly-trapped electrons must be explored, as well as the mechanisms that can fill those regions of phase space. Other radial electric potential profiles and initial distribution functions than semi-Maxwellian populations can be investigated. The effect of background electrons approaching from infinity can be easily included in the model, affecting the previously-empty regions and the free electron regions, as these are both connected to the downstream boundary condition. Finally, the mathematical properties of the model such as the general existence and uniqueness of solution should be discussed in more detail. A comparison with full-PIC codes and experiments, such as those of Ref. [17] will be carried out to confirm the range of validity of the model.

Acknowledgments

References

[1] Roy, R. I. S., Gastonis, N. a., and Hastings, D. E., "Ion-thruster plume modeling for backflow contamination," *Journal of Spacecraft and Rockets*, Vol. 33, No. 4, July 1996, pp. 525–534.

[2] Tverdokhlebova, E. and Korsun, A., "Plasma Plume/Spacecraft Interaction. State of the Art in Investigation Methodology," *Spacecraft Propulsion*, Vol. 465, 2000, p. 675.

[3] Tajmar, M., Gonzalez, J., and Hilgers, A., "Modelling of spacecraft-environment interactions on SMART-1," *JOURNAL OF SPACECRAFT AND ROCKETS*, Vol. 38, No. {3}year.

[4] Goebel, D. M. and Katz, I., *Fundamentals of Electric Propulsion: Ion and Hall Thrusters*, JPL, 2008.

[5] Garrett, H. and Whittlesey, A., "Spacecraft charging, an update," *Plasma Science, IEEE Transactions on*, Vol. 28, No. 6, 2000, pp. 2017–2028.

[6] Garrett, H. B. and Whittlesey, A. C., *Guide to mitigating spacecraft charging effects*, John Wiley & Sons, 2012.

[7] Leboeuf, J., Chen, K.-R., Donato, J., Geohegan, D., Liu, C., Puretzky, A., and Wood, R., "Modeling of plume dynamics in laser ablation processes for thin film deposition of materials," *Physics of Plasmas*, Vol. 3, No. 5, 1996, pp. 2203–2209.

[8] Lieberman, M. and Lichtenberg, A., *Principles of plasma discharges and materials processing*, Wiley-Blackwell, 2005.

[9] Lebedev, S., Ciardi, A., Ampleford, D., Bland, S., Bott, S., Chittenden, J., Hall, G., Rapley, J., Jennings, C., Sherlock, M., et al., "Production of radiatively cooled hypersonic plasma jets and links to astrophysical jets," *Plasma Physics and Controlled Fusion*, Vol. 47, No. 12B, 2005, pp. B465.

[10] Myers, R. and Manzella, D., "Stationary Plasma Trhuster Plume Characteristics," *23rd International Electric Propulsion Conference, Seattle, WA*, IEPC 93-096, 1993.

[11] Gallimore, A., "Near-and far-field characterization of stationary plasma thruster plumes," *Journal of Spacecraft and Rockets*, Vol. 38, No. 3, 2001, pp. 361–368.

[12] Beal, B., Gallimore, A., and W.A. Hargus, J. H., "Plasma Properties in the Plume of a Hall Thruster Cluster," *Journal of Propulsion and Power*, Vol. 20, No. 20, 2004, pp. 985 – 991.

[13] Foster, J. E., Patterson, M., Pencil, E., McEwen, H., Diaz, E., and Van Noord, J., "Plasma characteristics measured in the plume of a NEXT multi-thruster array," *42nd Joint Propulsion Conference*, 2006.

[14] Ekholm, J. M., Hargus, W. A., Larson, C. W., Nakles, M. R., Reed, G., and Niemela, C. S., "Plume characteristics of the

busek 600 w hall thruster," *Proceedings of the 42nd Joint Propulsion Conference and Exhibit, no. AIAA-2006-4659. American Institute of Aeronautics and Astronautics*, 2006.

[15] L. Brieda, M. N., D. R. Garrett, W. J. H., and Randy, R., "Experimental and Numerical Examination of the BHT-200 Hall Thruster Plume," *43rd AIAA/ASME/SAE/ASEE Joint Propulsion Conference & Exhibit*, AIAA, Washington DC, 2007.

[16] Dannenmayer, K., Mazouffre, S., Merino, M., and Ahedo, E., "Hall Effect Thruster Plasma Plume Characterization with Probe Measurements and Self-Similar Fluid Models," *48th AIAA/ASME/SAE/ASEE Joint Propulsion Conference & Exhibit*, No. AIAA-2012-4117, AIAA, Washington DC, 2012.

[17] Giono, G., Mazouffre, S., Loubere, D., Popelier, L., Théroude, C., Dannenmayer, K., Marguet, F., Gudmundsson, J. T., Ivchenko, N., Olentsenko, G., and Merino, M., "Experimental Determination of the Plasma Properties in the Far-plume of an SPT-100 Hall Thruster," *35th International Electric Propulsion Conference*, No. IEPC-2017-385, Electric Rocket Propulsion Society, Fairview Park, OH, 2017.

[18] Manzella, D., Jankovsky, R., Elliott, F., Mikellides, I., Jongeward, G., and Allen, D., "Hall thruster plume measurements on-board the Russian Express satellites," Tech. Rep. NASA/TM–2001-211217, 2001.

[19] Vicini, A., Passaro, A., and Biagioni, L., "Hall Thruster 3D Plume Modeling and Comparison with SMART-1 Flight Data," *4th International Spacecraft Propulsion Conference*, Vol. 555, 2004.

[20] Hilgers, A., Thiébault, B., Estublier, D., Gengembre, E., Del Amo, J. G., Capacci, M., Roussel, J.-F., Tajmar, M., and Forest, J., "A simple model of the effect of solar array orientation on SMART-1 floating potential," *IEEE transactions on plasma science*, Vol. 34, No. 5, 2006, pp. 2159–2165.

[21] Gabdullin, F., Korsun, A., and Tverdokhlebova, E., "The plasma plume emitted onboard the international space station under the effect of the geomagnetic field," *Plasma Science, IEEE Transactions on*, Vol. 36, No. 5, 2008, pp. 2207–2213.

[22] Estublier, D. L., "The SMART-1 spacecraft potential investigations," *IEEE Transactions on Plasma Science*, Vol. 36, No. 5, 2008, pp. 2262–2270.

[23] Aston, G., Kaufman, H., and Wilbur, P., "Ion beam divergence characteristics of two-grid accelerator systems," *AIAA Journal*, Vol. 16, 1978, pp. 516–524.

[24] Hofer, R. and Gallimore, A., "Recent results from internal and very-near-field plasma diagnostics of a high specific impulse Hall thruster," *28th International Electric Propulsion Conference*, 2003, pp. 17–21.

[25] Boyd, I. and Dressler, R., "Far field modeling of the plasma plume of a Hall thruster," *Journal of applied physics*, Vol. 92, No. 4, 2002, pp. 1764.

[26] Merino, M., Cichocki, F., and Ahedo, E., "Collisionless Plasma thruster plume expansion model," *Plasma Sources Science and Technology*, Vol. 24, No. 3, 2015, pp. 035006.

[27] Wang, J., Brinza, D., and Young, M., "Three-Dimensional Particle Simulation Modeling of Ion Propulsion Plasma Environment for Deep Space One," {*Journal of Spacecraft and Rockets*}.*volume*, , No. 3, 2001.

[28] Hu, Y. and Wang, J., "Electron Properties in Collisionless Mesothermal Plasma Expansion: Fully Kinetic Simulations," *Plasma Science, IEEE Transactions on*, Vol. 43, No. 9, 2015, pp. 2832–2838.

[29] Kahnfeld, D., Schneider, R., Cichocki, F., Merino, M., Ahedo, E., Duras, J., and Koch, N., "Comparison of plume simulations of a 2D3V-PIC-MCC and a 3D Hybrid-PIC code," *35th International Electric Propulsion Conference*, No. IEPC-2017-329, Electric Rocket Propulsion Society, Fairview Park, OH, 2017.

[30] Korsun, A., Tverdokhlebova, E., and Gabdullin, F., "Simulation of plasma plume-to-spacecraft interaction," *Computer physics communications*, Vol. 164, No. 1, 2004, pp. 353–364.

[31] Ortega, A. L., Katz, I., Mikellides, I. G., and Goebel, D. M., "Self-Consistent Model of a High-Power Hall Thruster Plume," *IEEE Transactions on Plasma Science*, Vol. 43, No. 9, 2015, pp. 2875–2886.

[32] Oh, D. Y., "Computational modeling of expanding plasma plumes in space using a PIC-DSMC algorithm," *25th International Electric Propulsion Conference, Cleveland, OH*, No. IEPC-97-179, 1997.

[33] VanGilder, D. B., Font, G. I., and Boyd, I. D., "Hybrid Monte Carlo-particle-in-cell simulation of an ion thruster plume," *Journal of Propulsion and Power*, Vol. 15, No. 4, 1999, pp. 530–538.

[34] Brieda, L., Pierru, J., Kafafy, R., and Wang, J., "Development of the draco code for modeling electric propulsion plume interactions," *40th AIAA/ASME/SAE/ASEE Joint Propulsion Conference and Exhibit*, 2004, p. 3633.

[35] Wartelski, M., Theroude, C., Ardura, C., and Gengembre, E., "Self-consistent Simulations of Interactions Between Spacecraft and Plumes of Electric Thrusters," *33th International Electric Propulsion Conference*, No. IEPC-2013-73, 2013.

[36] Taccogna, F., Pagano, D., Scortecci, F., and Garulli, A., "Three-dimensional plume simulation of multi-channel thruster configuration," *Plasma Sources Science and Technology*, Vol. 23, No. 6, 2014, pp. 065034.

[37] Araki, S. J., Martin, R. S., Bilyeu, D. L., and Koo, J. W., "SM/MURF: Current Capabilities and Verification as a Replacement of AFRL Plume Simulation Tool COLISEUM," *52nd AIAA/SAE/ASEE Joint Propulsion Conference*, 2016, p. 4939.

[38] Cichocki, F., Domínguez, A., Merino, M., and Ahedo, E., "A 3D hybrid code to study electric thruster plumes," *Space Propulsion Conference 2016*, No. 3124968, European Space Agency, Rome, Italy, 2016.

[39] Boyd, I. and Yim, J., "Modeling of the near field plume of a Hall thruster," *Journal of applied physics*, Vol. 95, 2004, pp. 4575.

[40] Passaro, A., Vicini, A., and Biagioni, L., "3D computation of plasma thruster plumes," *40th AIAA/ASME/SAE/ASEE Joint Propulsion Conference & Exhibit*, AIAA, Washington DC, 2004.

[41] Merino, M., Proux, A., Fajardo, P., and Ahedo, E., "Collisionless electron cooling in unmagnetized plasma thruster plumes," *52th AIAA/ASME/SAE/ASEE Joint Propulsion Conference & Exhibit*, No. AIAA 2016-5037, AIAA, Salt Lake City, UT, 2016.

[42] Martinez-Sanchez, M., Navarro-Cavallé, J., and Ahedo, E., "Electron cooling and finite potential drop in a magnetized plasma expansion," *Physics of Plasmas*, Vol. 22, No. 5, 2015, pp. 053501.

[43] Correyero Plaza, S., Navarro, J., and Ahedo, E., "Expansion of a collisionless magnetized plasma plume with bi-Maxwellian electrons," *52nd AIAA/SAE/ASEE Joint Propulsion Conference*, 2016, p. 5035.

[44]Sanchez-Arriaga, G., Zhou, J., Ahedo, E., Martinez-Sanchez, M., and Ramos, J., "One-dimensional Direct Vlasov Simulations of Non-stationary Plasma Expansion in Magnetic Nozzle," 35th *International Electric Propulsion Conference*, No. IEPC-2017-106, Electric Rocket Propulsion Society, Fairview Park, OH, 2017.

[45]Goldstein, H., Poole, C. P., and Safko, J. L., *Classical mechanics*, Pearson, 2001.

[46]Merino, M. and Mauriño, J., "Akiles2d code: Advanced Kinetic Iterative pLasma Expansion Solver 2D," 2017.

A.   Computation of moments of the electron distribution function

Following the enumeration of the electron subpopulations given in Section A, the ijk-th moment of electron distribution function f_e at a point (z, r) of the plume for the l-th electron subpopulation is given by:

$$\mathcal{M}_{ijk(l)}(z,r) = \iiint \bar{f}_{e(l)} v_z^i v_r^j v_\theta^k \, d\boldsymbol{v}, \tag{40}$$

where the integral extends to all phase space. The total ijk-th moment for the full electron species is then

$$\mathcal{M}_{ijk} = \mathcal{M}_{ijk(1)} + \mathcal{M}_{ijk(2)} + \mathcal{M}_{ijk(4)}. \tag{41}$$

Reflected electrons (subpopulation 2) and doubly-trapped electrons (4) do not contribute to odd moments in v_z, which depend only on the free electrons (1). Also as $\bar{f}_e$ is independent of β_r, it is symmetric in v_r, and for a non-rotating plume, $\bar{f}_e$ is also symmetric in v_θ. Hence, the integral vanishes for odd j or k.

Several derived quantities are commonly defined from the distribution function moments and are used in the text. As in Eq. (41), a subindex in parenthesis, if present, denotes a single electron subpopulation, and when dropped, refers to the full electron species. Electron densities are

$$n_{e(l)} = \mathcal{M}_{000(l)}. \tag{42}$$

Axial velocities are defined as:

$$u_{ze(l)} = \frac{\mathcal{M}_{100(l)}}{n_{e(l)}}, \tag{43}$$

with $u_{ze(2)} = u_{ze(4)} = 0$. Note that $u_{ze(1)} \neq u_{ze}$ as it is weighted with a different density. The temperature tensor is diagonal, with

$$T_{ze(l)} = m_e \left(\frac{\mathcal{M}_{200(l)}}{n_{e(l)}} - u_{ze(l)}^2 \right), \tag{44}$$

$$T_{re(l)} = T_{\theta e(l)} \equiv T_{\perp e(l)} = m_e \frac{\mathcal{M}_{020(l)}}{n_{e(l)}}. \tag{45}$$

The average temperature is defined as $T_{e(l)} = (T_{ze(l)} + 2T_{\perp e(l)})/3$. Observe that $n_e T_{ze} \neq \sum n_{e(l)} T_{ze(l)}$ due to the u_{ze}^2 term. Finally, higher moments can be defined likewise.

In the case of a radially-parabolic electric potential as in Section III, the even moments of the distribution function in v_r and v_θ for the l-th electron subpopulation can be computed as the following triple integral in the $E, p_\perp, p_\theta$ variables,

$$\mathcal{M}_{ijk(l)}(h,r) = \frac{1}{r^{k+1}} \frac{\sqrt{2^{i+j+3}T_e^*}}{\sqrt{m_e^{i+j+2k+5}}} \frac{h_0}{h^2} \int dE \int dp_\perp \left[E - U_{\text{eff}}(h, p_\perp) \right]^{\frac{i-1}{2}} \int dp_\theta \ldots$$
$$\left(\sqrt{\frac{2T_e^*}{m_e}} \frac{h_0}{h^2} p_\perp - \frac{T_e^* h_0^2}{h^4} r^2 - \frac{p_\theta^2}{2m_e r^2} \right)^{\frac{j-1}{2}} p_\theta^k \left[\bar{f}_{e(l)}^+ + (-1)^i \bar{f}_{e(l)}^- \right], \tag{46}$$

which has an avoidable singularity at the plume axis, $r = 0$. In this expression, the integral on p_θ runs from 0 to $r[2\sqrt{2T_e^* m_e} h_0 p_\perp / h^2 - 2T_e^* m_e h_0^2 r^2 / h^4]^{1/2}$, the integral on $p_\perp$ from $[\sqrt{T_e^* m_e / 2} h_0 r^2 / h^2]$ to $p_{\perp M}$, and the integral on E from $[-e\phi_z(h) + T_e^* h_0^2 r^2 / h^4 (z)]$ to ∞.

Lastly, if the distribution function at the upstream boundary condition is semi-Maxwellian as in Eq. (28), the integral simplifies to:

$$\mathcal{M}_{ijk(l)}(z,r) = 2n_{e0}^+ \sqrt{\left(\frac{2T_e^*}{m_e} \right)^{i+j+k}} \frac{\Gamma\left(\frac{1+j}{2}\right) \Gamma\left(\frac{1+k}{2}\right)}{2\pi^{3/2} \, \Gamma\left(1 + \frac{j+k}{2}\right)} \exp\left(\frac{e\phi_z(h)}{T_e^*} - \frac{h_0^2}{h^4} r^2 \right) \int_0^\infty g_{ijk(l)}(\mathcal{E}) \exp(-\mathcal{E}) \, d\mathcal{E}, \tag{47}$$

with:

$$g_{ijk(l)}\left(\mathcal{E}\right) = \int_0^{\mathcal{E}} \mathcal{P}_l\left(h, E, p_\perp\right) \sqrt{\left(\mathcal{E} - \mathcal{E}_\perp\right)^{i-1} \mathcal{E}_\perp^{j+k}} \mathrm{d}\mathcal{E}_\perp, \tag{48}$$

where $\mathcal{P}_l\left(h, E, p_\perp\right)$ is equal to 1 for passing electron regions, $1 + (-1)^i$ for reflected electron regions, and $\alpha[1 + (-1)^i]$ for doubly trapped regions; and

$$\mathcal{E} = \frac{1}{T_e^*}\left[E + e\phi_z(h)\right] - \frac{h_0^2}{h^4}r^2, \tag{49}$$

$$\mathcal{E}_\perp = \sqrt{\frac{2T_e^*}{m_e}} \frac{h_0}{h^2} \frac{p_\perp}{T_e^*} - \frac{h_0^2}{h^4}r^2. \tag{50}$$

The integral of Eq. (48) can be reduced in each region of phase space to hypergeometric functions.

B. Additional analysis of phase space geometry

In the radially-parabolic potential case of Section III, the different regions of phase space are defined by Eq. (25). As explained in Section III, for each h, this equation defines a straight line $s(h)$,

$$s(h): E + e\phi_z(h) - \sqrt{\frac{2T_e^*}{m_e}} \frac{h_0}{h^2} p_\perp = 0. \tag{51}$$

For $h = h_0$ and $h \to \infty$ this line takes the form

$$s(h_0): E - \sqrt{\frac{2T_e^*}{m_e}} \frac{p_\perp}{h_0} = 0, \tag{52}$$

$$s(\infty): E + e\phi_\infty = 0, \tag{53}$$

where $\phi_\infty = \phi_z(\infty)$. When transformed into the velocity space at the plume axis, these lines become the following circle and curve, respectively:

$$s(h_0): v_z^2 + v_r^2\left(1 - \frac{h^2}{h_0^2}\right) - \frac{2e}{m_e}\phi_z(h) = 0, \tag{54}$$

$$s(\infty): v_z^2 + v_r^2 - \frac{2e}{m_e}\left(\phi_z(h) - \phi_\infty\right) = 0. \tag{55}$$

The extent of the free electron region is closely linked to the electron current in the plasma plume, the value of ϕ_∞, and the ratio n_{e0}^+/n_{e0}^-. This region coincides with the space above $s(h_0)$ and $s(\infty)$, as long as there exist no intermediate barriers of U_{eff} that reduce its extent. According to Eq. (25), this condition is met when the solution $\phi_z(h)/\phi_\infty$ satisfies

$$\frac{\phi_z(h)}{\phi_\infty} \leqslant 1 - \frac{h_0^2}{h^2} \tag{56}$$

for all values of h,. Condition (56) is plotted on Fig. 3(a). If this inequality is verified, the quasineutrality and current-free Eqs. (18) at $h = h_0$ fully determine ϕ_∞ and n_{e0}^-/n_{e0}^+. For a semi-Maxwellian population at the upstream boundary as in Eq. (28),

$$\frac{n_{i0}}{n_{e0}^+} = 1 + \mathrm{erf}\sqrt{\frac{-e\phi_\infty}{T_e^*}} - \sqrt{\frac{2}{\pi}}\sqrt{\frac{-e\phi_\infty}{T_e^*}}\exp\left(\frac{e\phi_\infty}{T_e^*}\right),$$

$$\chi\frac{n_{i0}}{n_{e0}^+} = \sqrt{\frac{2}{\pi}}\left(1 - \frac{e\phi_\infty}{T_e^*}\right)\exp\left(\frac{e\phi_\infty}{T_e^*}\right), \tag{57}$$

where χ is the normalized ion velocity parameter defined in Section III.